Auto-Correction of Nonanechoic Antenna Measurements Based on Multitaper Approach

Mariusz Dzwonkowski and Adrian Bekasiewicz, *Senior Member, IEEE*

***Abstract*—Measurements of antenna prototypes are normally performed in dedicated yet costly environments such as anechoic chambers (ACs). However, the AC construction cost might be unjustified when the measurements aim to support education or budget-tight research. Alternatively, experiments can be realized in a nonanechoic regime and refined using appropriate methods. In this letter, a framework for the correction of antenna far-field measurements performed in uncontrolled environments based on the multitaper concept has been proposed. The method involves extracting a direct transmission between the measurement system components, while reducing undesirable factors such as noise and interferences. The performance of the approach has been demonstrated based on a total of 16 tests of two small antennas performed in nonanechoic conditions. The framework has also been compared against the methods from the literature.**

***Index Terms*—Antenna measurements, compact antennas, multitaper method, nonanechoic tests, radiation pattern.**

I. Introduction

EXPERIMENTAL validation is of pivotal importance for antenna development. It normally involves assessing the electrical- and field-related performance metrics in facilities such as anechoic chambers (ACs), open-test environments, or compact-range sites [1], [2]. Despite offering high accuracy, the cost associated with the construction of such laboratories may not be justified for applications such as teaching or research with tight budgets. The cost of antenna validation can be reduced by neglecting the control over the radiation environment—maintained at professional facilities—in favor of experiments in nonanechoic sites such as office cubicles or courtyards [3], [4], [5], [6]. Unfortunately, due to interferences and noise, the mentioned conditions are unsuitable for drawing meaningful conclusions on the far-field performance of the antenna under test (AUT).

Manuscript received 12 February 2024; accepted 28 February 2024. Date of publication 5 March 2024; date of current version 4 December 2024. This work was supported in part by the National Science Centre of Poland under Grant 2021/43/B/ST7/01856; in part by the National Centre for Research and Development under Grant NOR/POLNOR/HAPADS/0049/2019-00; and in part by Gdansk University of Technology (Excellence Initiative – Research University) under Grant 16/2023/IDUB/IV.2/EUROPIUM. *(Corresponding author: Adrian Bekasiewicz.)*

Mariusz Dzwonkowski is with the Faculty of Electronics, Telecommunications and Informatics, Gdansk University of Technology, 80-233 Gdańsk, Poland, and also with the Department of Radiology Informatics and Statistics, Faculty of Health Sciences, Medical University of Gdansk, 80-210 Gdańsk, Poland.

Adrian Bekasiewicz is with the Faculty of Electronics, Telecommunications and Informatics, Gdansk University of Technology, 80-233 Gdańsk, Poland (e-mail: bekasiewicz@ru.is).

Digital Object Identifier 10.1109/LAWP.2024.3372992

Nonanechoic measurements accuracy can be improved through post-processing oriented toward (1) characterization of the propagation environment or (2) signal decomposition [3], [4], [5], [6], [7], [8], [9], [10], [11], [12], [13], [14], [15], [16], [17]. The former involves neglecting the effects of the environment on a line-of-sight (LoS) transmission between the reference antenna (RA) and AUT based on redundant measurements [4], [5], [6], [7], [8], [9], [10]. Examples include reconfigurations of the test site [4], [5], determination of the environmental noise levels [7], evaluation of correlations between ideal and more practical test sites [9], [10]. The second group of methods implements spectral or time-domain analyses to extract LoS signals [11], [12], [13], [14], [15], [16]. The concept involves approximation of far-field responses using a composition of basis functions [13], [14], [15], [16], or truncation of the impulse response using carefully selected window functions [6], [13], [14], [15], [16]. Unfortunately, the applicability of the mentioned approaches to uncontrolled environments is limited due to their cognition-based (and problem-specific) tuning. Furthermore, the existing algorithms are predominantly validated in idealized environments (ACs, semi-ACs) using large, high-gain radiators. From this perspective, a reliable correction of far-field antenna responses in uncontrolled conditions remains an open issue.

In this letter, a framework for correction of far-field measurements conducted in nonanechoic test site that exploits multitaper wavelets has been proposed. The taper kernels are tuned using numerical optimization to automatically amplify the significant portion of the signal while suppressing the noise and interferences. The method has been validated using two geometrically small antennas dedicated to sensor applications (e.g., a radiological system that could be used for breast cancer detection) [19], [20]. A total of 16 experiments that span across nine unique frequencies have been performed. The method has been verified against state-of-the-art techniques.

II. Methodology

A. Problem Formulation

Let $\boldsymbol{R}_u(\boldsymbol{\omega}, \boldsymbol{\theta})$ represent the nonanechoic, far-field responses of the RA-AUT system. Here, $\boldsymbol{\omega} = [\omega_1 \ \ldots \ \omega_k]^T$, $k = 1, \ldots, K$, is a frequency sweep around $f_0 = B/2$, where bandwidth $B = \omega_K - \omega_1$; $\boldsymbol{\theta} = [\theta_1 \ \ldots \ \theta_a]^T$, $a = 1, \ldots, A$, is the vector of AUT angles w.r.t. RA. Interferences and electromagnetic (EM) noise make $\boldsymbol{R}_u(\boldsymbol{\omega}, \boldsymbol{\theta})$ inadequate for drawing conclusions on the AUT performance. Let $\boldsymbol{R}_c(f_0, \boldsymbol{\theta})$ be the refined AUT response at f_0 as a function of $\boldsymbol{\theta}$. The correction process involves extraction of $\boldsymbol{R}_c(f_0, \boldsymbol{\theta})$—that approximates AC measurements—using multitaper-based wavelet kernels applied to short-time events extracted from the $\boldsymbol{R}_u(\boldsymbol{\omega}, \boldsymbol{\theta})$ data.

© 2024 The Authors. This work is licensed under a Creative Commons Attribution 4.0 License. For more information, see https://creativecommons.org/licenses/by/4.0/

B. Multitaper Method for a Short-Time Event

A multitaper post-processing balances the resolution and variance of the signal [21], [22], [23]. The method introduces a set of orthogonal functions, so-called discrete prolate spheroidal sequences (DPSSs) [24]. DPSS can be used to construct low-bias, statistically consistent estimators optimized to reduce spectral leakage [21], [22], [23], [24], [25], [26]. The method is applied to a series of segmented, short-time events extracted from $\boldsymbol{R}_u(\boldsymbol{\omega}, \boldsymbol{\theta})$ as follows. Let $\boldsymbol{T}_u = \boldsymbol{T}_u(\boldsymbol{t}, \theta_a) = F^{-1}(\boldsymbol{R}_u, N)$ be the complex N-point ($N = 2^{\lceil \log_2 K \rceil + 3}$) time-domain response obtained at θ_a angle using inverse Fourier transform (denoted as $F^{-1}(\cdot)$), where $\boldsymbol{R}_u = \boldsymbol{R}_u(\boldsymbol{\omega}, \theta_a)$ [27]. The time span is $\boldsymbol{t} = [t_1, \ldots, t_N]^T = \partial t \cdot \boldsymbol{M} - \Delta t_a$, where $\partial t = B^{-1} \cdot (K-1)/(N-1)$, and $\boldsymbol{M} = [-m, \ldots, m-2, m-1]^T$, and $m = N/2$; Δt_a represents temporal shift of the LoS power pulse w.r.t. $t = 0$ at θ_a angle. The impulse response $\boldsymbol{T}_u$ can be confined into a series of short-time $\boldsymbol{T}_{u.k} = \boldsymbol{T}_u(\tau_k, \theta_a)$ intervals, where $\tau_k = [\tau_1, \ldots, \tau_k, \ldots, \tau_K]^T$ and $\tau_k = t_{m-\lfloor K/2 \rfloor + k}$ (the symbols $\lceil \cdot \rceil$, $\lfloor \cdot \rfloor$ denote round-up, -down to the nearest integer). Now let $\boldsymbol{T}_\sigma = \boldsymbol{T}_{u.k}(\boldsymbol{t}_\sigma, \theta_a)$ be the σ-th segment of $\boldsymbol{T}_{u.k}$, such that $\boldsymbol{t}_\sigma = \partial t \cdot \boldsymbol{M}_\sigma$, where $\boldsymbol{M}_\sigma = [\mu_\sigma, \ldots, \mu_\sigma + n - 1]^T$, $\mu_\sigma = -\lfloor K/2 \rfloor + (\sigma - 1) \cdot s$ and $\sigma = 1, 2, \ldots, \lfloor (K - n + s)/s \rfloor$. The parameter $n = 1, 2, \ldots, K-1$ refers to the segment length (defined in points) of the short-time event $\boldsymbol{T}_{u.k}$. The parameter $s = 1, 2, \ldots, n$ refers to the step size (points-wise) for the subsequent segments of $\boldsymbol{T}_{u.k}$. Note that $n - s$ measures a potential overlap between subsequent segments, and therefore, for $s = n$, consecutive $\boldsymbol{T}_\sigma$ do not overlap. Additionally, for $n = 1$ (and thus $s = 1$), there will be K segments of $\boldsymbol{T}_{u.k}$, each being of unit length (i.e., a single discrete time-instance), while for $n = K-1$, there will be either one segment for $s > 1$ or two segments with $K-2$ overlapping points (for $s = 1$). Here, $1 \leq s \leq n \leq K/2$ is assumed. Overlapping the segments offers temporal interpolation of data that could increase the precision of spectral event identification [21].

The post-processing involves modification (i.e., multiple tapering) of the individual $\boldsymbol{T}_\sigma$ segments with a series of DPSS-based wavelet kernels

$$\boldsymbol{R}_\sigma(\boldsymbol{\Omega}_\sigma, \theta_a) = \sum_{w=0}^{q} F(\boldsymbol{T}_\sigma \circ \boldsymbol{T}_{\kappa c}(\boldsymbol{t}_\sigma, w), n) \cdot \lambda_w \tag{1}$$

where "$F(\cdot)$" and "$\circ$" are the n-point Fourier transform and component-wise multiplication. The sweep $\boldsymbol{\Omega}_\sigma = \partial\omega \cdot \boldsymbol{M}_\sigma$ for $\partial\omega = (t_N - t_1)^{-1}$, whereas q is the overall number of kernels; λ_w ($w = 0, \ldots, q$), and $\boldsymbol{T}_{\kappa c}(\boldsymbol{t}_\sigma, w)$ denotes normalized weighting factor, and wth DPSS-based wavelet kernel of the form

$$\boldsymbol{T}_{\kappa c}(\boldsymbol{t}_\sigma, w) = \boldsymbol{T}_\kappa(\boldsymbol{t}_\sigma, w) \circ e^{j2\pi B \cdot \boldsymbol{t}_{sin}}. \tag{2}$$

The vector $\boldsymbol{t}_{sin} = [t_{m-\lfloor n/2 \rfloor}, \ldots, t_{m-\lfloor n/2 \rfloor + n - 1}]^T$ and the wth DPSS function $\boldsymbol{T}_\kappa(\boldsymbol{t}_\sigma, w)$ is identified by solving

$$\xi_w \cdot \boldsymbol{T}_\kappa(\boldsymbol{t}_\sigma^{(\gamma)}, w) = \sum_{\rho=0}^{n-1} \frac{\sin(2\pi(\gamma - \rho) \cdot W)}{\pi(\gamma - \rho)} \cdot \boldsymbol{T}_\kappa(\boldsymbol{t}_\sigma^{(\rho)}, w). \tag{3}$$

Here, ρ and $\gamma = 0, 1, \ldots, n-1$ and ξ_w is the energy concentration of the wth sequence. The problem (3) involves finding the n-point-long, finite energy time sequence that maximizes the ratio of spectral concentration for the given bandwidth $2W$ (which defines a resolution of the multitaper method) [21], [26]. Note that the coefficient $W = v \cdot (n \cdot \partial t)^{-1}$, where v is the time-half-bandwidth (THB) and the ratio $v/n < 0.5$. DPSS functions and their concentrations can be identified as eigenvectors and their corresponding eigenvalues of the n-by-n self-adjoint positive semidefinite operator [28], [29], [30], [31].

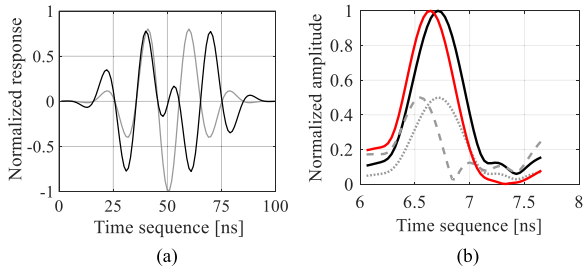

Fig. 1. Multitaper-based correction in time-domain representation: (a) real-part of the normalized DPSS-based wavelet kernels ($\partial t = 1$ ns) of order $w = 0$ (gray), $w = 1$ (—) for $n = 100$ and $\nu = 4$, as well as (b) example segment of the short-time event for the AUT response measured at θ_a before (black), during (gray) and after (red) refinement. Note that the correction has been performed using two DPSS-based wavelet kernels with equal weights; hence, the max amplitude of both tapered segment responses (gray) is 0.5.

The proposed wavelet variant of DPSSs (2) ensures the complex nature of the kernel functions used for tapering segments. A time-domain visualization of normalized characteristics obtained for the first two wavelet DPSSs [real part generated according to (2)], and the example segment correction are depicted in Fig. 1.

Upon solving (1) for all $\boldsymbol{T}_\sigma$ segments, the resulting response $\boldsymbol{R}_c(\boldsymbol{\Omega}, \theta_a)$ is yielded as a concatenation of all subsequent $\boldsymbol{R}_\sigma(\boldsymbol{\Omega}_\sigma, \theta_a)$ responses with applied arithmetic mean for overlapping indices. Note that $\boldsymbol{\Omega} = \partial\omega \cdot \boldsymbol{M}_\omega$, where $\boldsymbol{M}_\omega = [-\lfloor K/2 \rfloor, \ldots, -\lfloor K/2 \rfloor + (\lfloor (K - n + s)/s \rfloor - 1) \cdot s + n - 1]^T$. The corrected nonanechoic transmission between the components of the RA-AUT system at $f_0 \in \boldsymbol{\Omega}$ (note that $\boldsymbol{\omega} \in \boldsymbol{\Omega}$) and the θ_a angle is extracted as $R_c(f_0, \theta_a)$. Consequently, the determination of the $\boldsymbol{R}_c(f_0, \boldsymbol{\theta})$ involves the execution of the above-outlined procedure for all $\boldsymbol{\theta}$ angles.

C. Optimization of Multitaper Parameters

Determination of appropriate $\boldsymbol{R}_\sigma(\boldsymbol{\Omega}_\sigma, \theta_a)$ involves numerical optimization. Let $\boldsymbol{x} = [\boldsymbol{x}_I, \boldsymbol{x}_F]^T$, where $\boldsymbol{x}_I = [n\ s]^T$ and $\boldsymbol{x}_F = [v\ \lambda]^T$ be the discrete- and floating-point vectors that control DPSS parameters, whereas $\boldsymbol{\lambda} = [\lambda_0\ \ldots\ \lambda_w\ \ldots\ \lambda_q]^T$, $w = 0, \ldots, q$, denotes the vector of their weighting factors (cf. Section II-B). The optimized design is found as a result of the constrained, mixed-integer minimization process

$$\boldsymbol{x}^* = \arg \min_{\substack{1 \leq s \leq n \leq n_{\max},\ n > 1 \\ 0 < v < v_u}} (U(\boldsymbol{x})) \tag{4}$$

where $U(\boldsymbol{x}) = -R_c(f_0, \theta_{\text{init}}, \boldsymbol{x}) = -R_c(f_0, \theta_{\text{init}}, [\boldsymbol{x}_I, \boldsymbol{x}_F]^T)$ is a scalar objective function, whereas $\boldsymbol{x}$ in R_c is used to express that the control parameters are devolved to (1)–(3). The angle θ_{init} represents a position of the AUT w.r.t. RA at which the minimization of (4) has been performed. The weighting coefficients are bounded to a range of $0.1 \leq \lambda_w \leq 0.9$ and $q = \max\{\lfloor v_u \rfloor, 1\}$. The algorithm is as follows:

1. Set $j = 0$, $U_{\text{best}} = 0$, and define the initial design $\boldsymbol{x}_I^{(j)}$;
2. Generate L perturbations $\{\boldsymbol{x}_{I.1}\ \ldots\ \boldsymbol{x}_{I.L}\}$ around $\boldsymbol{x}_{I.0} = \boldsymbol{x}_I^{(j)}$ using star-distribution design of experiment, set $l = 0$;
3. Set $\boldsymbol{x}_{F.l}^{(0)} = [0.5 q_l\ \boldsymbol{\lambda}_l]^T$, where $\lambda_{l.w} = 0.5$;
4. Find $\boldsymbol{x}_{F.l}^*$ by solving (4) using a gradient-based method;
5. If $U(\boldsymbol{x}_l^*) < U_{\text{best}}$, where $\boldsymbol{x}_l^* = [\boldsymbol{x}_{I.l}\, \boldsymbol{x}_{F.l}^*]$, set $\boldsymbol{x}_{\text{best}} = \boldsymbol{x}_l^*$, $U_{\text{best}} = U(\boldsymbol{x}_l^*)$, $\boldsymbol{x}_I^{(j+1)} = \boldsymbol{x}_l^*$, $j = j + 1$ and go to step 2; otherwise go to step 6;

MOST WIEDZY Downloaded from mostwiedzy.pl

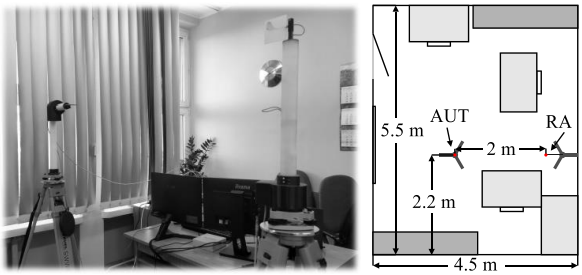

Fig. 2. Nonanechoic test site considered for experiments: (a) photograph and (b) schematic view with a highlight on the location of rotary towers, as well as tall cabinets (dark gray) and desks (light gray).

6. If $l = L$, set $\boldsymbol{x}^* = \boldsymbol{x}_{\text{best}}$ and END; otherwise, set $l = l+1$ and go to step 3.

The above method can be summarized as a gradient routine nested in a greedy-type, discrete hill-climbing algorithm. Typically, only a handful of steps is required to find $\boldsymbol{x}^*$, and the numerical cost of optimization is negligible compared to data acquisition (measurements). Note that L is the dimensionality of $\boldsymbol{x}_I$ vector. The design $\boldsymbol{x}_I^{(0)}$ can either be generated randomly or defined manually by setting small n, s values. The nonequality constraint in (4) is $v_u = 0.5(n–1)$, whereas the upper bound on n—that affects the number of DPSS tapers used for post-processing—is set to $n_{\max} = 15$. Although the assumed upper limit for $n_{\max}$ is $K/2$, the experiments indicate that a relatively low number of tapers is sufficient for correction.

D. Summary of the Framework

The proposed multitaper-based correction framework can be summarized as follows:

1. Set f_0, K, B, N, and measure $\boldsymbol{R}_u(\boldsymbol{\omega}, \boldsymbol{\theta})$ data;
2. Find $\boldsymbol{x}^*$ using the algorithm of Section II-C to extract the optimal DPSS wavelets using (2) and (3);
3. Calculate (1) for all $\boldsymbol{T}_\sigma$ segments of the short-time event;
4. Find $\boldsymbol{R}_c(\boldsymbol{\Omega}, \theta_a)$ and extract a-th element $R_c(f_0, \theta_a)$ of $\boldsymbol{R}_c(f_0, \boldsymbol{\theta})$ vector;
5. If $a = A$, END; otherwise, set $a = a+1$ and go to Step 3.

The resulting $\boldsymbol{R}_c(f_0, \boldsymbol{\theta})$ vector represents the corrected, far-field AUT response as a function of $\boldsymbol{\theta}$. Note that the above-discussed method exploits one-shot measurements, whereas DPSS parameters are optimized without engineering insight. Consequently, the approach represents a notable advancement compared to conventional post-processing that relies on the manual setup of algorithms [11], [12], [13], [14].

III. Correction Results

The performance of the proposed framework has been validated using two geometrically small antennas, i.e., an antipodal Vivaldi and a spline-based monopole [6], [32]. The reference responses for both structures have been obtained in the AC, while the nonanechoic measurements have been performed in a $5.5 \times 4.5 \times 3.1$ m^3 test site, presented in Fig. 2. The room is considered unsuitable for far-field experiments. Note that the Vivaldi structure serves as the reference antenna (RA) in the considered test setup. The angular resolution for the AUT movement is set to 5°, whereas $K = 201$ and B are both selected based on the rules-of-thumb [6], [11], [14]. For all of the considered experiments, the correction performance between nonanechoic and AC-based measurements is expressed in terms of a root-mean-square error e_R (in dB) defined as follows [6], [12]:

$$e_R(\boldsymbol{R}) = \left(\frac{1}{A} \sum_{a=1}^{A} \left(R_0(f_0, \theta_a) - R(f_0, \theta_a) \right)^2 \right)^{0.5} \tag{5}$$

where $e_R(\boldsymbol{R}) = e_R(\boldsymbol{R}(f_0,\boldsymbol{\theta}))$. The matrix $\boldsymbol{R}_0 = \boldsymbol{R}_0(f_0,\boldsymbol{\theta})$ represents the AC data, whereas $\boldsymbol{R}$ denotes the nonanechoic response of interest (i.e., before or after correction).

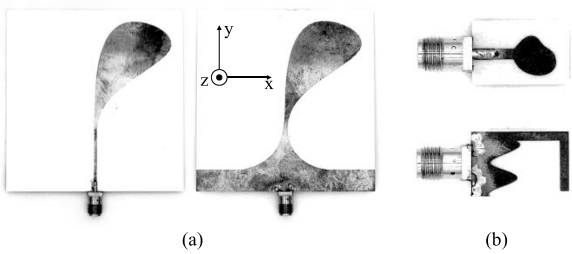

Fig. 3. Photographs (not in scale) of compact antenna structures used for experiments: (a) antipodal Vivaldi and (b) monopole.

TABLE I
Antipodal Vivaldi: Post-Processing Results

f_0 [GHz]	3.5	4.5	5.5	6.5	7.5	8.5	9.5	10.5	11.5
$e_R(\boldsymbol{R}_u)$ [dB]	–13.4	–13.8	–13.2	–15.3	–13.7	–16.7	–16.6	–14.7	–15.4
$e_R(\boldsymbol{R}_c)$ [dB]	–26.1	–23.1	–22.6	–26.7	–23.0	–22.5	–24.8	–25.2	–23.9
Δ [dB]	12.7	9.3	9.4	11.4	9.3	5.8	8.2	10.5	8.5

A. Case Study: Vivaldi

Consider a spline-based antipodal Vivaldi antenna shown in Fig. 3(a). The structure far-field radiation response (yz-plane) has been measured in the nonanechoic test site of Fig. 2 at the frequencies: $f_0 \in \{3.5, 4.5, 5.5, 6.5, 7.5, 8.5, 9.5, 10.5, 11.5\}$ GHz. The bandwidth around f_0 is set to $B = 1$ GHz [6]. The correction process has been performed according to the methodology outlined in Section II. First, the optimum DPSS parameters have been obtained using the algorithm of Section II-C. To ensure the operation of the algorithm in a deterministic regime, the initial design $\boldsymbol{x}_I^{(0)} = [6\ 6]^T$ has been set for all of the considered tests instead of using randomly generated samples. The parameter $\theta_{\text{init}} = 0°$ corresponds to the RA-AUT position at the beginning of the measurements, i.e., with the antennas facing each other in the (expected) direction of maximum gain. Upon minimization of (4), the optimized DPSS-based wavelets have been used to extract the refined $\boldsymbol{R}_c(f_0, \boldsymbol{\theta})$ responses (cf. Section II-B).

Table I comprises the antenna performance characteristics before and after correction calculated using (5). The obtained results indicate that, for the considered structure, the improvement of measurement fidelity due to post-processing, expressed as $\Delta = |e_R(\boldsymbol{R}_c) - e_R(\boldsymbol{R}_u)|$, varies from 5.8 dB at 8.5 GHz to 12.7 dB at 3.5 GHz. The average and median improvement of the performance w.r.t. AC responses amount to almost 9.5 dB (i.e., from –14.8 dB before to –24.2 dB after correction) and 9.3 dB, respectively. A comparison of the antenna responses at 3.5 GHz ($\boldsymbol{x}^* = [13\ 6\ 1.02\ 0.08\ 0.75\ 0.08\ 0.08]^T$; cf. Section II-C) and 10.5 GHz ($\boldsymbol{x}^* = [13\ 12\ 5.99\ 0.08\ 0.08\ 0.08\ 0.75]^T$) frequencies is shown in Fig. 4. The presented results demonstrate that

MOST WIEDZY Downloaded from mostwiedzy.pl

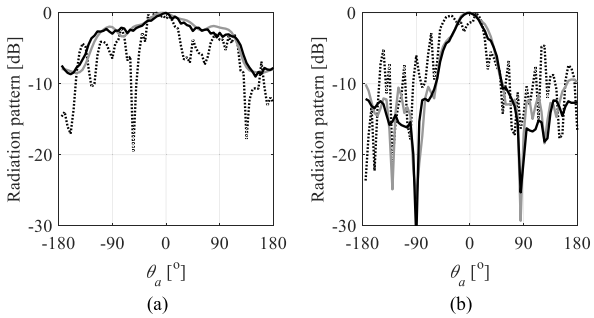

Fig. 4. Comparison of AC (gray) and non-AC (black) patterns of the Vivaldi antenna before (···) and after (—) correction: (a) 3.5 and (b) 10.5 GHz.

TABLE II
SPLINE MONOPOLE: POST-PROCESSING RESULTS

f_0 [GHz]	3.5	4.5	5.5	6.5	7.5	8.5	9.5
$e_R(\boldsymbol{R}_u)$ [dB]	–6.96	–10.3	–14.1	–15.9	–7.06	–15.5	–10.3
$e_R(\boldsymbol{R}_c)$ [dB]	–30.3	–25.6	–22.6	–19.2	–14.5	–28.4	–15.2
Δ [dB]	23.3	15.3	8.5	3.3	7.44	12.9	4.9

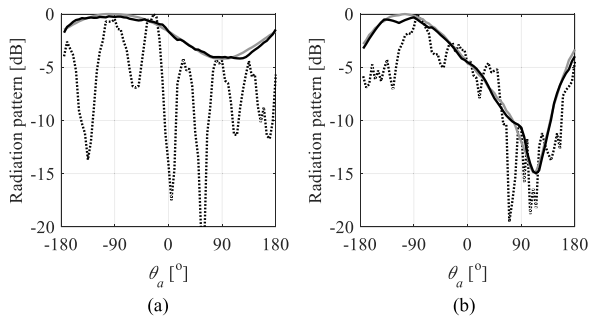

Fig. 5. Comparison of AC (gray) and non-AC (black) patterns of the spline monopole before (···) and after (—) correction: (a) 3.5 and (b) 8.5 GHz.

improvement of the antenna far-field radiation patterns due to the proposed correction is notable.

B. Case Study: Spline Monopole

Our second example is a spline-based monopole of Fig. 3(b) [6]. The antenna non-anechoic measurements (yz-plane) have been performed at $f_0 \in \{3.5, 4.5, 5.5, 6.5, 7.5, 8.5, 9.5\}$ GHz frequencies ($B = 3$ GHz) and corrected using the methodology of Section II with $\boldsymbol{x}_I^{(0)} = [6\ 6]^T$. The post-processing results are summarized in Table II, whereas Fig. 5 shows a comparison (w.r.t. AC characteristics) of the radiation patterns—before and after correction—obtained at 3.5 GHz ($\boldsymbol{x}^* = [9\ 6\ 1.15\ 0.1\ 0.9]^T$) and 8.5 GHz ($\boldsymbol{x}^* = [9\ 6\ 1.15\ 0.1\ 0.9]^T$). The refined far-field responses are characterized by substantially improved fidelity w.r.t. AC-based data—i.e., from 3.3 dB at 6.5 GHz to 23.3 dB at 3.5 GHz—compared to the uncorrected measurements. In summary, the average e_R increased by 10.8 dB, transitioning from –11.4 dB to –22.3 dB (w.r.t. AC measurements). Note that, a relatively gradual, decline of the correction performance with frequency might be due to deterioration of the signal-to-noise ratio resulting from both low antenna gain and increased contribution of S_{21} uncertainty to the low-amplitude signals (as $|S_{21}|$ is roughly around –70 dB for $f > 7$ GHz).

TABLE III
BENCHMARK OF THE PROPOSED FRAMEWORK

AUT	Correction method performance (average e_R [dB])*				
	(i)	(ii)	(iii)	(iv)	This work
Section III.*A*	–20.9	–21.1	–22.6	–21.7	–24.2
Section III.*B*	–15.2	–14.4	–16.5	–16.5	–22.3

* Averaged over all of the considered antenna-specific test frequencies.

IV. DISCUSSION AND COMPARISONS

The presented framework has been compared against the state-of-the-art correction algorithms. The benchmark includes three time-domain methods where signal intervals for window functions are based on (i) manual estimation of direct RA-AUT distance (2 m) and the reflected path (4.1 m), (ii) experience-driven analysis of the impulse response (12 ns and 10 ns for antennas of Fig. 3(a) and (b), respectively), and (iii) the application of a generic composite window adjusted according to thresholds w.r.t. the impulse response [7], [11], [12]. For unbiased comparison, the $\boldsymbol{R}_u$ datasets and f_0, K, B, and N parameters used for post-processing are consistent across all of the benchmarks and set in accordance with the discussion of Section III. The proposed technique has also been compared against the matrix-pencil approach (iv), which is dedicated to spectral-based refinement [10]. The pencil parameter and the number of exponentials have been set to $K/3$ and 2, respectively [14]. Note that, for all benchmark algorithms except (iii), the setup has been determined manually. The results collected in Table III (averaged across the frequency points pertinent to the given antennas) indicate that—for the considered test environment—the proposed approach offers the best correction performance (often by a large margin). Improvement of the refined radiation patterns due to the application of the proposed algorithm is up to 9.1 dB when compared to the benchmark methods. The obtained results show that the proposed framework is not only capable of ensuring a high correction performance but also discards the experience-driven setup of post-processing in favor of automatic tuning based on rigorous numerical optimization.

V. CONCLUSION

In this letter, a new framework for auto-correction of antenna far-field measurements performed in challenging, nonanechoic conditions was proposed. The method exploits optimized sets of DPSS-based wavelet kernels to augment a series of short-time responses of the RA-AUT system obtained from one-shot measurements. The process is oriented towards enhancing the useful fraction of the signal while suppressing interferences due to multi-path propagation and external EM noise. The method performance was thoroughly validated using two geometrically small antennas measured in nonanechoic site in the form of an office room (considered unsuitable for such tests). A total of 16 experiments that span over nine unique frequencies were performed. On average, the application of the proposed post-processing leads to an improvement of results fidelity by around 10 dB compared to the uncorrected signals. The framework has been benchmarked against the approaches from the literature.

Future work will focus on optimization for the automatic determination of the bandwidth around the frequency of interest so as to maximize the correction performance based on a thorough and systematic analysis of propagation conditions rather than rule-of-thumb approaches.

MOST WIEDZY Downloaded from mostwiedzy.pl

REFERENCES

[1] L. Hemming, *Electromagnetic Anechoic Chambers: A Fundamental Design and Specification Guide*. Piscataway, NJ, USA: IEEE Press, 2002.

[2] S. Kurokawa, M. Hirose, and K. Komiyama, "Measurement and uncertainty analysis of free-space antenna factors of a log-periodic antenna using time-domain techniques," *IEEE Trans. Instrum. Meas.*, vol. 58, no. 4, pp. 1120–1125, Apr. 2009.

[3] P. Piasecki and J. Strycharz, "Measurement of an omnidirectional antenna pattern in an anechoic chamber and an office room with and without time domain signal processing," in *Proc. Signal Process. Symp.*, Debe, Poland, 2015, pp. 1–4.

[4] M. D. Migliore, "Filtering environmental reflections in far-field antenna measurement in semi-anechoic chambers by an adaptive pattern strategy," *IEEE Trans. Antennas Propag.*, vol. 52, no. 4, pp. 1112–1115, Apr. 2004.

[5] S. M. Froes, P. Corral, M. S. Novo, M. Aljaro, and A. C. C. Lima, "Antenna radiation pattern measurement in a nonanechoic chamber," *IEEE Antennas Wireless Propag. Lett.*, vol. 18, no. 2, pp. 383–386, Feb. 2019.

[6] A. Bekasiewicz, S. Koziel, and M. Czyz, "Time-gating method with automatic calibration for accurate measurements of electrically small antenna radiation patterns in non-anechoic environments," *Measurement*, vol. 208, 2023, Art. no. 112477.

[7] A. N. de Sao Jose, V. Deniau, U. C. Resende, and R. Adriano, "Improving antenna gain estimations in non-ideal test sites with auto-tunable filters," *Measurement*, vol. 159, 2020, Art. no. 107720.

[8] J. Knapp, J. Kornprobst, and T. F. Eibert, "Equivalent source and pattern reconstruction from oversampled measurements in highlyreflective environments," *Microw., Antennas Propag.*, vol. 13, no. 13, pp. 2232–2241, 2019.

[9] J. Koh, A. De, T. K. Sarkar, H. Moon, W. Zhao, and M. Salazar-Palma, "Free space radiation pattern reconstruction from non-anechoic measurements using an impulse response of the environment," *IEEE Trans. Antennas Propag.*, vol. 60, no. 2, pp. 821–831, Feb. 2012.

[10] T. K. Sarkar, M. Salzar-Palma, M. D. Zhu, and H. Chen, *Modern Characterization of Electromagnetic Systems and Its Associated Metrology*. Hoboken, NJ, USA: Wiley, 2021.

[11] S. Loredo, M. R. Pino, F. Las-Heras, and T. K. Sarkar, "Echo identification and cancellation techniques for antenna measurement in non-anechoic test sites," *IEEE Antennas Propag. Mag.*, vol. 46, no. 1, pp. 100–107, Feb. 2004.

[12] A. Soltane, G. Andrieu, E. Perrin, C. Decroze, and A. Reineix, "Antenna radiation pattern measurement in a reverberating enclosure using the time-gating technique," *IEEE Antennas Wireless Propag. Lett.*, vol. 19, no. 1, pp. 183–187, Jan. 2020.

[13] B. Fourestie, Z. Altman, J. Wiart, and A. Azoulay, "On the use of the matrix-pencil method to correlate measurements at different test sites," *IEEE Trans. Antennas Propag.*, vol. 47, no. 10, pp. 1569–1573, Oct. 1999.

[14] G. Leon, S. Loredo, S. Zapatero, and F. Las-Heras, "Radiation pattern retrieval in non-anechoic chambers using the matrix pencil algorithm," *Prog. Electromagn. Res. Lett.*, vol. 9, pp. 119–127, 2009.

[15] Z. Du, J. I. Moon, S.-S. Oh, J. Koh, and T. K. Sarkar, "Generation of free space radiation patterns from non-anechoic measurements using Chebyshev polynomials," *IEEE Trans. Antennas Propag.*, vol. 58, no. 8, pp. 2785–2790, Aug. 2010.

[16] B. Fourestie and Z. Altman, "Gabor schemes for analyzing antenna measurements," *IEEE Trans. Antennas Propag.*, vol. 49, pp. 1245–1253, Sep. 2001.

[17] T. M. Gemmer and D. Heberling, "Accurate and efficient computation of antenna measurements via spherical wave expansion," *IEEE Trans. Antennas Propag.*, vol. 68, no. 12, pp. 8266–8269, Dec. 2020.

[18] J. Mroczka, "The cognitive process in metrology," *Measurement*, vol. 46, pp. 2896–2907, 2013.

[19] S. C. Hagness, A. Taflove, and J. E. Bridges, "Two-dimensional FDTD analysis of a pulsed microwave confocal system for breast cancer detection: Fixed-focus and antenna-array sensors," *IEEE Trans. Biomed. Eng.*, vol. 45, no. 12, pp. 1470–1479, Dec. 1998.

[20] M. Lu, X. Xiao, Y. Pang, G. Liu, and H. Lu, "Detection and localization of breast cancer using UWB microwave technology and CNN-LSTM framework," *IEEE Trans. Microw. Theory Techn.*, vol. 70, no. 11, pp. 5085–5094, Nov. 2022.

[21] M. J. Prerau et al., "Sleep neurophysiological dynamics through the lens of multitaper spectral analysis," *Physiol. (Bethesda)*, vol. 32, no. 1, pp. 60–92, 2017.

[22] T. Bronez, "On the performance advantage of multitaper spectral analysis," *IEEE Trans. Signal Process.*, vol. 40, no. 12, pp. 2941–2946, Dec. 1992.

[23] D. B. Percival and A. T. Walden, *Spectral Analysis for Physical Applications: Multitaper and Conventional Univariate Techniques*. Cambridge, U.K., MA, USA: Cambridge Univ. Press, 1993.

[24] M. X. Cohen, *Analyzing Neural Time Series Data: Theory and Practice*. Cambridge, MA, USA: MIT Press, 2014.

[25] D. J. Thomson, "Spectrum estimation and harmonic analysis," *Proc. IEEE*, vol. 70, no. 9, pp. 1055–1096, Sep. 1982.

[26] B. Babadi and E. N. Brown, "A review of multitaper spectral analysis," *IEEE Trans. Biomed. Eng.*, vol. 61, no. 5, pp. 1555–1564, May 2014.

[27] A. V. Oppenheim and R. W. Schafer, *Discrete-Time Signal Processing*, 3rd ed., Englewood Cliffs, NJ, USA: Prentice-Hall, 2009.

[28] D. Slepian, "Prolate spheroidal wave functions, fourier analysis, and uncertainty – V: The discrete case," *Bell Syst. Tech. J.*, vol. 57, no. 5, pp. 1371–1430, 1978.

[29] D. T. Hristopulos, "Discrete prolate spheroidal sequence," in *Encyclopedia of Mathematical Geosciences, Encyclopedia of Earth Sciences Series*, B.S. Daya Sagar, Eds., Cham, Germany: Springer, 2021.

[30] K. S. Riedel and A. Sidorenko, "Minimum bias multiple taper spectral estimation," *IEEE Trans. Signal Process.*, vol. 43, no. 1, pp. 188–195, Jan. 1995.

[31] E. J. McCoy, A. T. Walden, and D. B. Percival, "Multitaper spectral estimation of power law processes," *IEEE Trans. Signal Process.*, vol. 46, no. 3, pp. 655–668, Mar. 1998.

[32] J. Bai, S. Shi, and D. W. Prather, "Modified compact antipodal Vivaldi antenna for 4–50-GHz UWB application," *IEEE Trans. Microw. Theory Techn.*, vol. 59, no. 4, pp. 1051–1057, Apr. 2011.

MOST WIEDZY Downloaded from mostwiedzy.pl